



Mechanistic insight into electron orientation by tailoring Ni–Cu atom-pairs for high-performance CO₂ electroreduction

Yi Shen^{a,*}, Haizhong Zhang^a, Baoliang Chen^b, Chao Zhu^{a,*}, Weiting Yu^a, Jingyi Yang^a, Qile Fang^c, Zhiqiao He^a, Tulai Sun^d, Shuang Song^{a,*}

^a Key Laboratory of Microbial Technology for Industrial Pollution Control of Zhejiang Province, College of Environment, Zhejiang University of Technology, Hangzhou 310032, PR China

^b Department of Environmental Science, Zhejiang University, Hangzhou 310058, PR China

^c Advanced Institute of Natural Sciences, Beijing Normal University at Zhuhai, Zhuhai 519087, PR China

^d Center for Electron Microscopy, State Key Laboratory Breeding Base of Green Chemistry Synthesis Technology, Zhejiang University of Technology, Hangzhou 310032, PR China

ARTICLE INFO

Keywords:

Electron orientation
Double-atom catalyst
Electrocatalysis
Protonation
Carbon dioxide reduction

ABSTRACT

The electrochemical CO₂ reduction reaction (CO₂RR) is a promising solution for addressing global issues related to carbon neutrality and energy shortage. However, it is hindered by the high thermal stability of CO₂ and competitive hydrogen evolution reaction, which lead to low efficiency and selectivity. Herein, a Ni–Cu atom-pair catalyst with well-defined electron orientation has been tailored for electrocatalytic CO₂RR. In particular, the tailored Ni/Cu_{0.38}-covalent triazine framework catalyst exhibited extremely high catalytic activity with high faradaic efficiency (99.82% at –1.1 V vs. reversible hydrogen electrode, RHE) and turnover frequency (5116 h^{–1} at –1.1 V vs. RHE). To the best of our knowledge, this is a diatomic catalyst with the lowest reported metal concentration and excellent efficiency and selectivity. Density functional theory calculations and experimental results further revealed that the adsorption of CO₂ was enhanced, while the electron orientation from the Cu site to Ni site reduced the antibonding orbital coupling between Ni and C atoms in CO₂, thereby breaking the protonation energy barrier and providing high catalytic efficiency. Moreover, the enrichment of electrons from the electrolyte as well as the accumulation of *H at Cu sites was essential for improving CO selectivity.

1. Introduction

Continuous increase in CO₂ levels in the atmosphere has led to the greenhouse effect, causing various ecological and environmental problems, such as land desertification and sea-level rise. Consequently, converting and utilizing CO₂ to maintain a reasonable concentration remains an impending challenge. [1–3] Electrocatalytic reduction is a potential approach to address global carbon balance and energy production concerns since it can convert CO₂ to CO as fuel or other high-value products. [4,5] However, due to the competitive adsorption of H₂O in the electrolyte solution, the undesirable hydrogen evolution reaction (HER) occurs, resulting in low selectivity of the CO₂ reduction reaction (CO₂RR). [6] In addition, the high thermodynamic stability of CO₂ (bond energy of the C=O bond is ~750 kJmol^{–1}) makes it difficult to protonate or break bonds during the CO₂RR, resulting in low reduction efficiency. [7] Furthermore, the fast desorption of intermediates is

crucial for improving CO₂RR selectivity and performance. [8–10] Accordingly, improving the selectivity and efficiency of the CO₂RR is the present bottleneck.

Single-atom catalysts (SACs) exhibit 100% atomic utilization, flexible coordination structures, and excellent electronic properties, which are instrumental in improving the adsorption and desorption of various intermediates. [11–16] Owing to their excellent properties, researchers investigating the CO₂RR have shown considerable interest in SACs, where M–N–C (M = transition metal) has been developed as a classical conformation. [17–20] For instance, the atomically dispersed low-valent Ni(i) center had high intrinsic CO₂ reduction activity with up to 97% CO selectivity. [21] A covalent triazine framework (CTF) modified with the unsaturated coordination of 3d metal Co atoms considerably lowered the energy barrier of the reaction process by enhancing the adsorption energy of the intermediate, resulting in extremely high catalytic efficiency. [22] The pyrolysis of Ni particles

* Corresponding authors.

E-mail addresses: shenyi@zjut.edu.cn (Y. Shen), zhuchao@zjut.edu.cn (C. Zhu), ss@zjut.edu.cn (S. Song).

<https://doi.org/10.1016/j.apcatb.2023.122654>

Received 15 January 2023; Received in revised form 13 March 2023; Accepted 15 March 2023

Available online 16 March 2023

0926-3373/© 2023 Elsevier B.V. All rights reserved.

into Ni single atoms can significantly improve the activity and selectivity of the catalyst. [23] Although the achievements are more than that, some general questions about SACs remain to be overcome, such as, the problem of small contact area and relatively weak interaction between a single atom and a supporting material, whether the atomically active sites represent the highest intrinsic catalytic activity, and how to improve its intrinsic activity. In general, the coordination environment of isolated atoms is modified to improve catalytic performance. [24].

Based on the above general problems and modification methods, diatomic catalysts (DACs) have begun to emerge in recent years as extended family members of SACs. For example, individual Fe single-atom catalysts do not perform well in CO₂RR, but the orbital coupling between the Fe center and adjacent Ni atoms in NiFe-DACs, results in the change of orbital energy level. Besides, the unique electronic state of Fe atom reduces the free energy of the intermediate, thereby improving the CO₂RR performance. [25] The introduction of Cu atoms in CuFe-N₆-DACs yields synergistic metal and pyridine N active centers (CuFe-N₆), which are uniformly anchored to the carbon backbone and improve proton and electron transfer, making CO selectivity of more than 95%. [26] Moreover, the orbital coupling between Fe double sites in Fe₂-N-DACs can effectively reduce the energy gap between the anti-bonded state and the bonded state in *CO adsorption, thereby promoting the CO₂RR process. [27] This is a result of the synergistic electronic effect and the ability to overcome the stubborn limitations of the scaling relationship of catalytic activity. [28–30] However, conventional atom-pair catalysts have a random electron distribution and orientation, which is not favorable to the directional improvement of the specific features of an atom in the atom-pair. Accordingly, we must urgently investigate how to tailor atom-pair catalysts with a specific electron orientation and how one atom interacts with the other in the atom-pair, thus overcoming the limitation of catalytic activity to prepare a highly efficient and selective catalyst.

Herein, a tailored double-atom catalyst was designed by screening out Ni–Cu atom-pairs, which can maximize the breakthrough energy barriers of CO₂RR protonation and be effectively synthesized via a two-step impregnation method. The coordination environments of the two atoms were determined using high-angle annular dark field scanning transmission electron microscopy (HAADF-STEM) and extended X-ray absorption fine structure (EXAFS) analysis. To the best of our knowledge, this is a very efficient catalyst that provides excellent CO selectivity (99.82% at –1.1 V vs. RHE) and HER inhibitory effect (0.83% at –1.1 V vs. RHE) with the lowest metal content. Density functional theory (DFT) further revealed the effects of electron orientation. The presence of electron orientation from Cu to Ni enhanced adsorption by weakening antibonding orbital coupling between the Ni and C atoms in *CO₂, leaving the Cu atom electron-deficient. In addition, changes in the bond length of reaction intermediates and accumulation of *H at Cu sites were considered to be key factors for surpassing the protonation energy barrier and further accelerating the reaction. This study provides a new strategy and insight to overcome the technical challenges of CO₂ electroreduction using synergistic catalysis of atom-pairs.

2. Experimental section

2.1. Synthesis of catalysts

Firstly, 2,6-pyridinedicarbonitrile (2,6-DCPY, 100 mg) and powdery Ketjen black EC600JD (100 mg) were mixed with Zinc chloride anhydrous (ZnCl₂, 9 g) in a sealed vacuum ampoule. Subsequently the ampoule was heated to 400 °C at 3.3 °C min^{–1} and maintained that temperature for 40 h. CTF was obtained by thoroughly washing the product with de-ionized water, tetrahydrofuran (1 M), hydrochloric acid (HCl, 1 M) and aqueous ammonia (1 M). [22] And then, CTF was added to 20 mM aqueous solution of nickel chloride hexahydrate (NiCl₂·6 H₂O) and stirred at 25 °C for 12 h. The resulting substance was collected by centrifugation (10000 rpm for 5 min) and dried at 60 °C overnight in a

vacuum. Ni–CTF was obtained after being calcined at 600 °C for 2 h and washed with de-ionized water and HCl (1 M) to remove all unbound metal ions.

Cu–CTF was prepared by CTF using the same method as Ni–CTF by replacing 20 mM aqueous solution of NiCl₂·6 H₂O with 1.5 mM aqueous solution of copper chloride dihydrate (CuCl₂·2 H₂O). Ni/Cu–CTF was obtained by continuing to follow the preparation steps of Cu–CTF on the basis of the Ni–CTF prepared in the previous steps. To avoid generating unnecessary single Cu sites after the atom-pairs were formed, the second metal Cu was used at a lower concentration. At the same time, in order to explore a suitable Cu incorporation amount, Ni/Cu–DACs were prepared with gradient concentration (0.75 mM, 1.5 mM, 5 mM, 10 mM) aqueous solution of CuCl₂·2 H₂O. To facilitate the discussion, Ni/Cu–DACs were named according to the actual ratio of Ni/Cu atoms obtained from ICP-OES in the catalyst.

2.2. CO₂ reduction reaction measurements

Electrochemical measurements were performed using an electrochemical station (CHI760E, China) in a reactor with two electrode chambers (separated by an ion exchange membrane) and three electrodes. Carbon paper (1 cm × 2 cm) with catalyst and a Pt tablets (2 cm × 2 cm) served as the cathode and anode electrodes, respectively. A Ag/AgCl (3.5 M KCl) was used as the reference electrode. The fully dispersed catalyst ink was obtained by ultrasonic-vibrating the mixture of catalyst (3 mg), ethanol absolute (300 μL, YongDa, China) and nafion (50 μL, HeSen, China) for 30 min. The cathode electrodes were prepared by spreading catalyst ink (100 μL) evenly on carbon paper and drying in a vacuum overnight. The electrode potentials were converted from RHE based on: [31].

$$E(\text{vs. Ag/AgCl}) = E(\text{vs. RHE}) + 0.21\text{V} - 0.0591 \times \text{pH}$$

During the CO₂RR experiment, the electrolyte was a CO₂ saturated 0.1 M aqueous solution of KHCO₃ (120 mL in the cathode electrode chambers with 130 mL gas headspace, pH = 6.8). Before all CO₂RR test, the cathode chamber of the reaction unit was filled with CO₂ (99%), and continuous access to CO₂ ensured a stable concentration throughout the process. The gas products in the cathode chamber were measured online by gas chromatography (GC, Shimadzu, Japan). And liquid products in the cathode chamber were analyzed online by ion chromatography. Wherein, the calibration of CO₂ and H₂ were detected by diluting the corresponding gases with argon to different concentrations. The markings of liquid products were provided online by ion chromatography with sample solutions of different concentrations.

All electrochemical characterization was carried out in the unipolar chamber reactor and obtained by the corresponding method in the electrochemical station. The open-circuit voltage was the data measured after a stable period of time. The electrolyte used in the test was a CO₂ saturated 0.1 M aqueous solution of KHCO₃ and the CO₂ concentration was maintained during the reaction. In addition, the electrodes used are consistent with those used in the CO₂ reduction reaction test. The polarization curves were recorded with linear scan voltammetry (LSV). Nyquist plots were collected from 100 kHz to 100 MHz at an AC voltage of 5 mV. The circuit fitting diagram was obtained through ZView software. Cyclic voltammograms (CV) measurements were conducted at various scan rates (2, 4, 6, 8, 10, 12 mV s^{–1}) in the potential windows of open circuit voltage (± 0.1 V) (vs. Ag/AgCl). By plotting the Δ*j* (the difference between cathodic and anodic current density) against the scan rate at open circuit voltage (vs Ag/AgCl), the double layer capacitance (*C*_{dl}) can be obtained from the half of corresponding slope value.

Faraday efficiency (FE) calculation formula for a gas product was as follows: [32].

$$FE = \frac{q \times F \times v_i \times V \times 0.01}{22.4 \times v \times t \times I}$$

where q is the number of electrons transferred during the generation of the target product ($q = 2$ for H_2 and CO_2) per mole, F is Faraday constant ($F = 96485.3 \text{ C mol}^{-1}$), v_i is the peak area measured by gas chromatography, V is the volume of the headspace layer of the cathode chamber ($V = 130 \text{ mL}$), 0.01 is the calibration coefficient of the peak area, v is the standard peak area of the product gas measured by GC, t is the CO_2RR test reaction time (s), I is the average current at a constant potential (A).

The following is the formula for the partial current density of CO_2 :

$$J_{\text{CO}} = \frac{FE_{\text{CO}} \times I}{S}$$

where S is the geometric surface area of the cathode electrode sheet in the electrolyte (cm^2).

Turnover Frequency (TOF) for CO production can be obtained by following formula:[33].

$$\text{TOF} = \frac{J_{\text{CO}} \times M}{q \times F \times r \times m} \times 3600$$

where M is the relative atomic mass of metallic elements, r is the ratio of doping of the active atoms on the catalyst obtained by ICP-OES, m is the quality of the catalyst on the working electrode in the cathode chamber. For Ni/Cu-CTF, Both the Cu ($M = 63.6 \text{ g mol}^{-1}$) and Ni ($M = 58.7 \text{ g mol}^{-1}$) metals are considered active sites and calculate in it.

2.3. Characterization

Powder X-ray diffraction (XRD) measurements were performed on a SmartLab SE diffractometer using Cu targets (tube voltage: 40 kV, current: 30 mA). The functional group structure was measured by Fourier transform infrared spectroscopy (FT-IR). Inductively coupled plasma optical emission spectrometer (ICP-OES) results were obtained by assays from Agilent 5110 instruments. The morphology of samples was observed through a field emission scanning electron microscope (FE-SEM, HITACHI Regulus 8100) at an acceleration voltage of 15 kV. Sample topography was also observed using high-resolution transmission electron microscopy (HR-TEM, FEI, Tecnai G2 F30). Atomic-resolution HAADF-STEM, element mapping analysis and electron energy-loss spectroscopy (EELS) were performed using a state-of-the-art transmission electron microscope equipped with double (image and probe) spherical aberration (Cs) correctors (Thermo Scientific Spectra 300). The total specific surface area of the material was obtained by the Brunauer Emmett Teller method (BET). At a vacuum of 300°C , the sample was pretreated for 24 h using the Micro instrument Standard Degassing Station. Then the sample was subjected to nitrogen aspiration and desorption testing using a 4-stop automatic specific surface area analyzer of the American Micromeritics APSP2460 model under 77 K liquid nitrogen conditions. After the instrument analysis was completed, the isothermal suction and desorption curve was obtained. X-ray photoelectron spectroscopy (XPS) spectra were collected with an ESCALAB 250Xi instrument using an Al K α X-ray as an excitation source. Both the Ni K-edge and Cu K-edge spectra were recorded under fluorescence mode at the BL14W beamline in the Shanghai Synchrotron Radiation Facility (SSRF).

2.4. Computation details

All spin polarization calculations were realized by means of DFT using the Vienna Ab initio Simulation Package. [34,35] The interaction between the ion cores and valence electrons were performed by the projector augmented wave (PAW) method. [36] The electron exchange-correlation energy adopted the Perdew-Burke-Ernzerhof (PBE) within the generalized gradient approximation (GGA). [37,38] The Brillouin zone was sampled by the $1 \times 1 \times 1$ Monkhorst-Pack grid for all structure optimization, and the structure optimization was implemented by a kinetics 400 eV plane wave basis set cut-off energy.

The convergence threshold of structure relaxation for force per atom was set as 0.02 eV \AA^{-1} , for energy change was set as 10^{-5} eV . A large 15 \AA vacuum space was adopted to avoid the influence derive from the periodic boundary conditions.

To calculate the formation energies of potential Cu dimer structures, we used the equation:

$$E_f = E(\text{System}) - E(\text{Substrate}) - E(\text{Cu}) - E(\text{Ni})$$

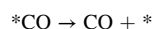
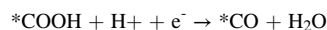
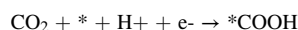
Here, E_f represents the formation energy of catalysts, $E(\text{System})$ represents the total free energy of the system, $E(\text{Substrate})$, $E(\text{Cu})$ and $E(\text{Ni})$ represent the free energies of the support, Cu atoms and Ni atoms.

The free energy graph is calculated using the concept of hydrogen electrode (CHE), in which the free energy of electron proton pair ($\text{H}^+ + \text{e}^-$) can refer to the chemical potential of gaseous hydrogen at equilibrium (0 V vs RHE). The free energy can be calculated as follows:

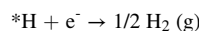
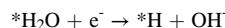
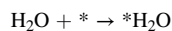
$$G = E + \text{ZPE} - TS$$

where E is the electronic energy directly obtained by DFT calculations. ZPE is the zero-point energy. T is the room temperature ($T = 298.15 \text{ K}$), and S is the entropy.

CO_2RR and HER are both considered in this work. The process of the CO_2 to CO consists of the following main steps:



And the splitting of water and the adsorption of H are considered.



3. Results and discussion

3.1. Theoretical prediction

Initially, DFT calculations were performed to determine the optimal atom-pair type. Because Ni-based catalysts exhibited excellent activity for CO_2 to CO conversion, Ni was selected as the preferred fixed metal. Accordingly, atom-pair catalysts were designed to help overcome the rate-determining step (RDS) limit of the first protonation in the CO_2RR process of SACs. A CTF was selected as the optimal substrate because its abundant N sites are suitable for coordination with transition metals, and pyridine N is particularly favorable to CO_2 adsorption. On this basis, pristine Ni-CTF (Fig. S1) and a series of Ni/M-CTFs (Fig. 1a, $M = \text{Ni, Fe, Co, or Cu}$) were constructed. As shown in Fig. 1b, the free energy changes of the catalytic conversion of $* \text{CO}_2$ to $* \text{COOH}$ over atom-pair catalysts (Ni/Ni-CTF, Ni/Fe-CTF, Ni/Co-CTF, and Ni/Cu-CTF) were calculated. Even though Ni-Fe was expected to surpass the limitations of the protonation RDS, it was reportedly poisoned by $* \text{CO}$. [33] Intriguingly, both Ni-Cu and Ni-Co surpassed the energy barrier, although Ni-Cu produced a greater reduction in free energy (-0.24 eV) than Ni-Co (-0.21 eV). Therefore, the Ni-Cu atom-pair was selected as the atom-pair type with the most advantageous protonation process characteristics. Secondly, the formation energy was calculated to evaluate the feasibility of the synthesis of Ni-Cu atom-pair catalysts (Table S1). Ni-SACs showed lower formation energy than Ni-DACs, suggesting that Ni atoms tended to form single-atom sites rather than Ni-Ni atom-pair sites during initial impregnation. Additionally, comparing the formation energies of Cu-SACs, Cu-DACs, and Ni/Cu-DACs suggests that Ni-Cu atom-pair sites form more stable sites than Cu single-atom sites and Cu-Cu atom-pair sites. Consequently, the Ni-Cu atom-pair catalyst

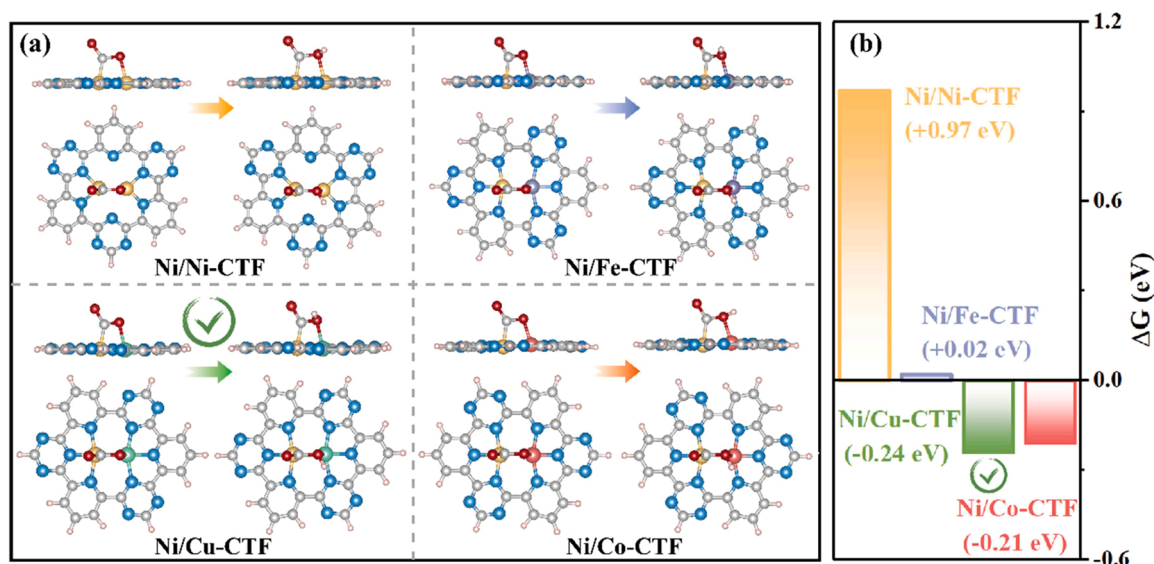


Fig. 1. (a) Optimized structural model and (b) Gibbs free energy variation of *CO_2 protonation process on Ni/Ni-CTF, Ni/Fe-CTF, Ni/Co-CTF, and Ni/Cu-CTF.

was not only the preferred catalyst for breaking past the first protonation energy barrier but it also became the most stable structure after two-step impregnation.

3.2. Characterization of Ni/Cu-CTF

The CTF was obtained through the polymerization of 2,6-DCPY via an ionothermal method. [22,39,40] DACs were synthesized via two-dip impregnation and annealing, as shown in Fig. 2a. The functional groups and crystal structure of the catalyst were examined before and after loading with metal atoms using FT-IR and XRD. According to the FT-IR spectra of the CTF, Ni-CTF, Cu-CTF, and Ni/Cu-CTF (Fig. 2b), the C=N stretching vibrational characteristic peak (at $\sim 2240\text{ cm}^{-1}$) of aromatic cyanide disappeared, indicating successful trimerization. Additionally, the presence of strong absorption peaks at 1220 and 1580 cm^{-1} confirmed the formation of triazine rings in the CTF, Ni-CTF, Cu-CTF, and Ni/Cu-CTF. [41] Subsequently, the metal compositions of the catalysts were analyzed using inductively coupled plasma mass spectrometry, which indicates that Ni/Cu elements were successfully incorporated into the CTF (Table S2). The catalysts were then named according to the ratio of the incorporated metal. For example, the catalyst with Ni and Cu concentrations of 0.28% and 0.10%, respectively, was denoted as Ni/Cu_{0.38}-CTF. Moreover, the XRD data (Fig. 2c) present a characteristic diffraction pattern of the CTF without any impurities. [42] The two peaks at approximately 25° and 44° corresponded to the (002) and (100) crystal faces of the graphite structure, respectively, indicating that the loading of Ni/Cu did not alter the crystal structure of the CTF. [43] More importantly, there were no peaks from crystalline metal oxides or metallic clusters, hence, it may be deduced that Ni/Cu existed in the atomic form.

Further, the morphological features of the catalysts were determined using FE-SEM and HR-TEM. As shown in Fig. 2d and Fig. S2, the morphology of the CTF is a slightly uneven layered structure with flocculent surfaces and edges. The rough surface possessed a large specific surface area and numerous exposed CO_2 adsorption sites, thereby establishing the structural prerequisites for subsequent metal doping and catalytic CO_2RR . With the incorporation of Ni atoms, the surface of the CTF tended to change from a flocculent to a layered structure. Furthermore, this change was completed after the $3d^{10}$ Cu atom was introduced. Comparisons between catalysts with varying Cu concentrations also suggested that this transition was not caused by multiple macerations or calcinations. Meanwhile, the transition was completed

when the Cu concentration reached the level of Ni/Cu_{0.38}-CTF. The transformation of catalyst morphology from the original chaotic stacking of pristine CTF to a regular layered structure of Ni/Cu-CTF allowed the interlayer active sites to be fully involved in the activation and catalysis of CO_2 . Furthermore, the catalyst sheet size in the HR-TEM image was primarily within 50 nm, with the monolayer structure in the translucent region being thinner. Moreover, energy-dispersive X-ray spectroscopy (Fig. 2e) revealed that the elements C, N, Ni, and Cu were uniformly distributed in Ni/Cu_{0.38}-CTF, confirming that Ni and Cu atoms were evenly distributed without aggregation on the catalyst.

The porous structure of the catalysts was analyzed further. As shown in Fig. S3 and Table S3, the BET specific surface area of the CTF was determined to be $1145\text{ cm}^2\text{g}^{-1}$, with a total pore volume of $2.62\text{ cm}^3\text{g}^{-1}$. With the incorporation of Ni atoms, the specific surface area and total pore volume of the CTF increased to $1264\text{ cm}^2\text{g}^{-1}$ and $2.86\text{ cm}^3\text{g}^{-1}$, respectively. Meanwhile, the incorporation of Cu atoms had a negative effect, causing the specific surface area and total pore volume of Ni/Cu_{0.38}-CTF to be intermediate between that of Cu-CTF and Ni-CTF. According to the pore diameters of various catalysts (Fig. S4), the pore sizes of all catalysts were concentrated between 3.6 nm and 3.9 nm, which were assigned to mesopores, except for the peak at $\sim 1.9\text{ nm}$ in Ni/Cu_{0.38}-CTF indicating the existence of newly-formed micropores. Mesopores facilitated mass transfer and micropores increased the density of active sites, thereby improving the overall catalytic activity of Ni/Cu_{0.38}-CTF. [44] Moreover, based on the N_2 adsorption-desorption curves, the hysteresis loops of all catalysts conformed to the H3 type, corresponding to a layered structure, which was consistent with the morphological characteristics observed via FE-SEM investigation.

HAADF-STEM was used to further reveal a more refined atomic structure of Ni/Cu_{0.38}-CTF. Metal clusters and oxidized nanoparticles were not observed in the Ni/Cu_{0.38}-CTF samples (Fig. 2f and Fig. S5). The spherical aberration-corrected HAADF-STEM image (Fig. S5b) revealed well-dispersed light spots $\sim 1.6\text{ \AA}$ in size. An abundance of atom-pairs was detected in the region marked by the orange circle. Moreover, statistical analysis of > 50 atom-pairs in different regions of the HAADF-STEM image of Ni/Cu_{0.38}-CTF (Fig. 2g, h) found that the average distance between two atoms in the atom-pair sites was $2.45 \pm 0.06\text{ \AA}$. Depending on the Z-contrast between atoms of various elements in the sample, it is possible to identify that the light spots in the image were Ni/Cu atoms. Accordingly, Ni/Cu was found to exist in Ni/Cu_{0.38}-CTF in a single-atom dispersed state. The bright dual dots were

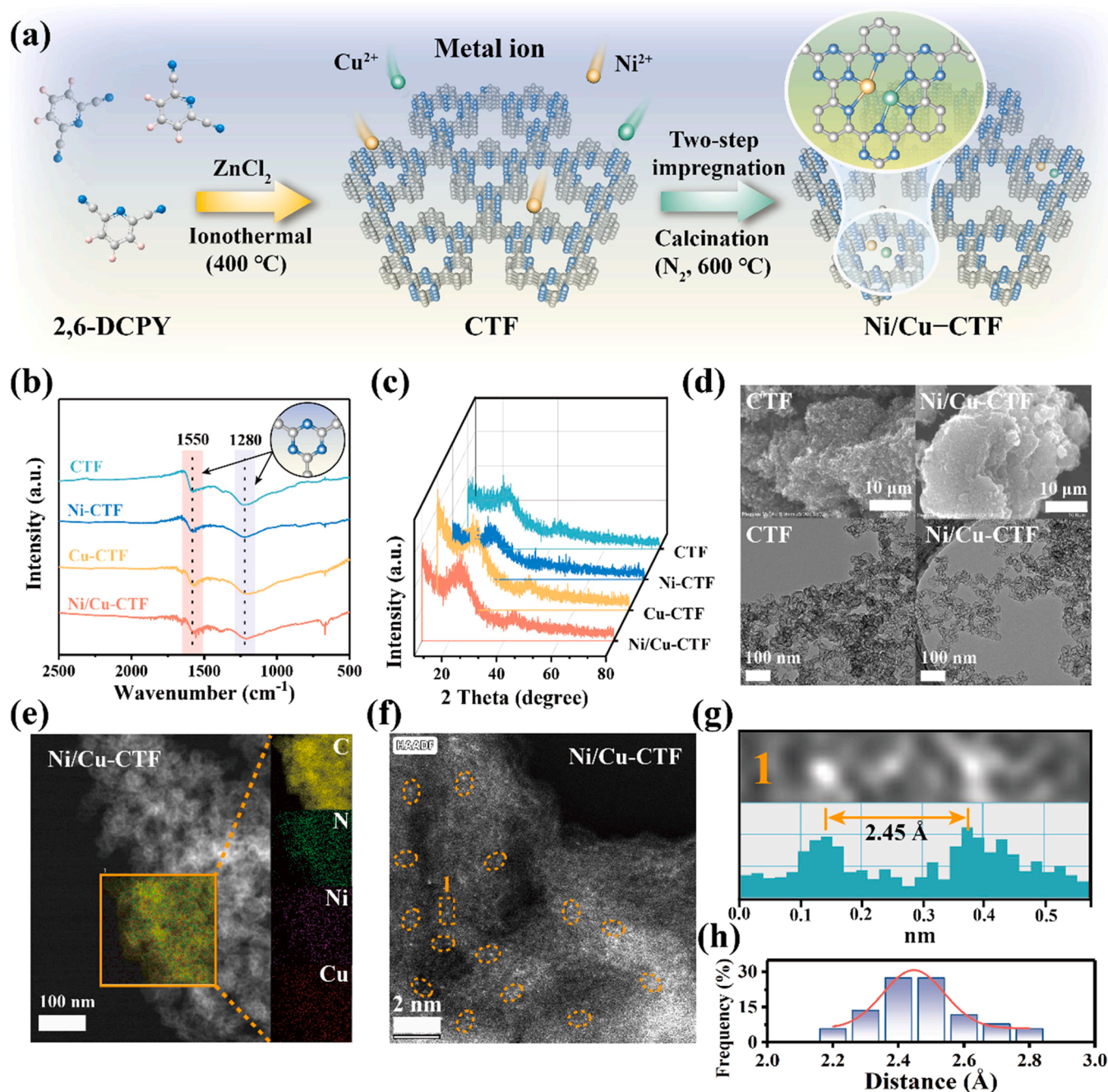


Fig. 2. (a) Schematic diagram of the synthesis of Ni/Cu-CTF. (b) FT-IR spectra, and (c) XRD pattern of CTF, Ni-CTF, Cu-CTF and Ni/Cu-CTF. (d) FE-SEM and HR-TEM images of CTF and Ni/Cu-CTF. (e) HR-TEM and corresponding EDXs mapping images of Ni/Cu-CTF. (f) Spherical aberration-corrected HAADF-STEM image corrected for Ni/Cu-CTF marked with orange circles. (g) Intensity profiles from the atomic pair site 1 in (f). (h) The lateral distance of the Ni and Cu atoms in the observed diatomic pairs.

further identified as Ni atom and Cu atom by EELS, which clearly indicated the formation of atom-pairs sites (Fig. S6). Even though classifying them as Ni-Cu atoms was desirable, conclusive confirmation was difficult as such images correspond to 2D projections of 3D structures. Additionally, they may be generated from Ni/Cu atoms that were widely separated in amorphous carbon but nearly overlapped in the imaging projection. [45].

To demonstrate the validity of the Ni-Cu atom-pairs, the valence states and local coordination structure of Ni and Cu atoms in Ni/Cu_{0.38}-CTF were examined using synchrotron X-ray absorption spectroscopy (XAS) and DFT calculations. [46] As shown in Fig. 3a, Ni K-edge X-ray absorption near-edge structure (XANES) revealed that the Ni

K-edge position (8343.26 eV) of Ni/Cu_{0.38}-CTF lay between that of NiO (8347.38 eV) and Ni foil (8340.84 eV). Furthermore, the Cu K-edge position of Ni/Cu_{0.38}-CTF is positioned between that of CuO and Cu₂O (Fig. 3b). According to additional fitting results (Fig. S7, S8) the oxidation states of Ni and Cu in Ni/Cu_{0.38}-CTF were 0.74 + and 1.82 +, respectively. Moreover, the local structure of Ni/Cu_{0.38}-CTF can be revealed using EXAFS spectroscopy (Fig. 3c, d). When compared with NiO and Ni foil, Ni/Cu_{0.38}-CTF showed no characteristic peaks corresponding to Ni-O and Ni-Ni bonds. Compared to NiPc, the highest peak of the first shell in Ni/Cu_{0.38}-CTF was assigned to Ni-N bonds, indicating that the majority of Ni atoms in Ni/Cu_{0.38}-CTF were coordinated with the N atoms. In contrast to CuO, Cu₂O, CuPc, and Cu foil, the peaks

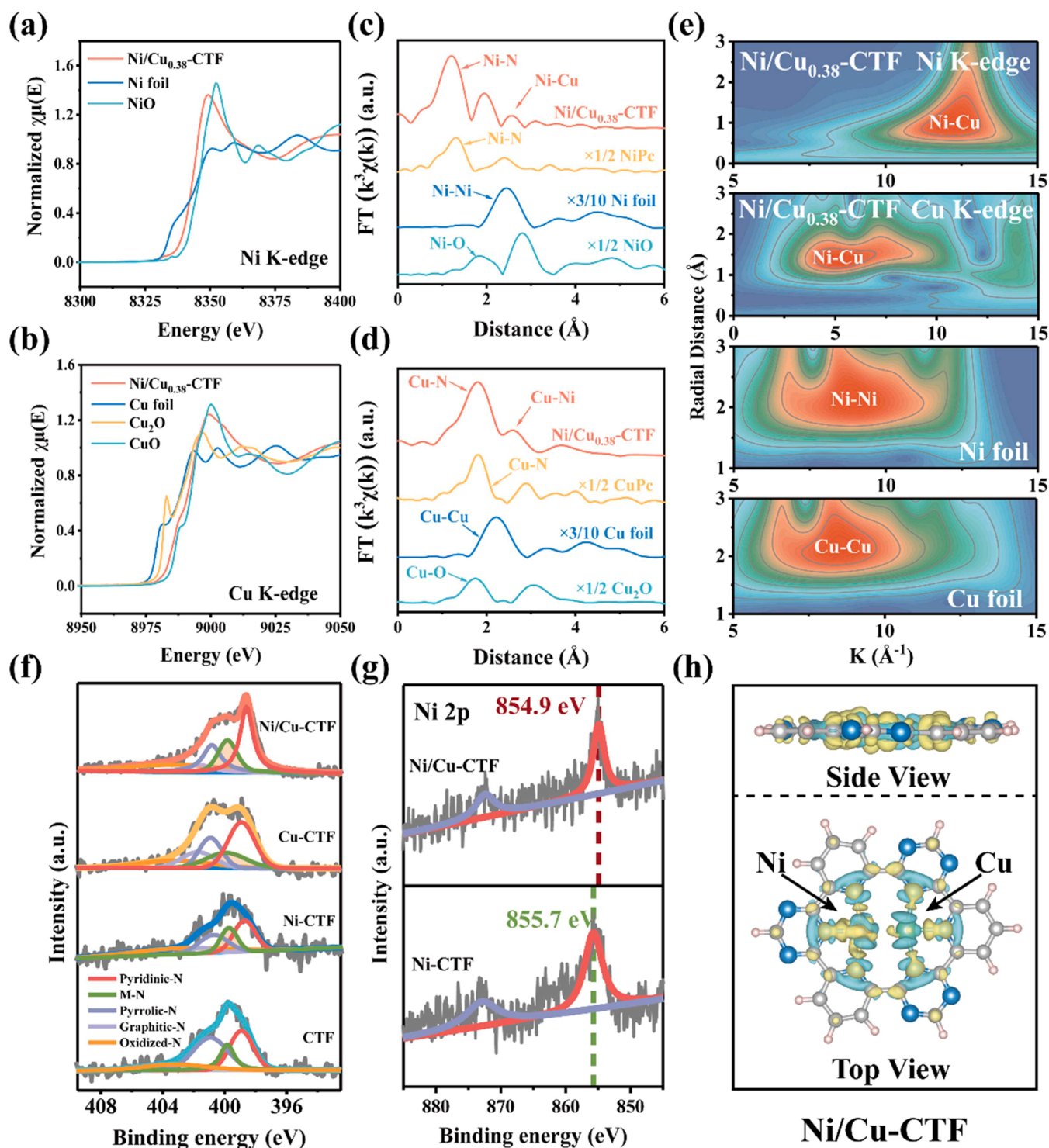


Fig. 3. (a) Ni K-edge and (b) Cu K-edge XANES spectra of the samples. (c) Ni K-edge and (d) Cu K-edge FT-EXAFS curves of the samples. (e) WT plots of Ni/Cu_{0.38}-CTF, Ni foil, and Cu foil. (f) High-resolution N 1s spectra. (g) High-resolution Ni 2p spectra. (h) The charge density difference distribution of Ni/Cu-CTF.

of the first shell were assigned to the Cu-N bond, indicating that neither Cu-O nor Cu-Cu bonds were present in Ni/Cu_{0.38}-CTF. In conjunction with HAADF-STEM, it was further confirmed that Ni and Cu atoms in Ni/Cu_{0.38}-CTF were dispersed atomically. Significantly, scattering paths at ~ 2.5 Å were both detected in the curves of Ni and Cu K-edge FT-EXAFS, which can be assigned to close interactions between Ni and Cu atoms. Wavelet transform (WT) with k and R space resolution was therefore employed to confirm the preceding conclusion. As observed in Fig. 3e and Fig. S9, the highest strength in the WT contour of

Ni/Cu_{0.38}-CTF did not match the Ni-Ni bond or the Ni-O bond, ruling out the presence of metallic nanoparticles and oxides. In addition, a similar result may be drawn from the WT-EXAFS of the Cu K-edge (Fig. S10). Moreover, the model-based EXAFS fitting of various metal K-edges (Table S4 and Fig. S11, S12) indicated that each Ni atom was coordinated with 2.6 N atoms and 0.8 Cu atoms, whereas each Cu atom was coordinated with 2.8 N atoms and 0.7 Ni atoms. The coordination number between Ni and Cu atoms was < 1 , indicating significant sub-nanometer-scale interaction. In addition, the distances of the Ni and

Cu atoms obtained via fitting were comparable to those obtained via statistical analysis in the HAADF-STEM images. Furthermore, optimized Ni/Cu_{0.38}-CTF structural model calculations (Fig. S13) showed that the distance between Ni and Cu atoms was 2.39 Å. Fitting and calculation results suggest that the circular highlights in Fig. 2f were Ni-Cu atom-pairs.

XPS was used to measure the surface composition and related electronic properties of the catalysts, as shown in Fig. S14–18, Table S5, and Fig. 3f, g. The peaks at 398.9, ~399.9, ~401.7, and ~403.2 eV in the N 1 s spectrum correspond to pyridinic N, pyrrolic N, graphitic N, and oxidized N, respectively. [47–52] Moreover, for the metal-incorporated CTF, the near-pyrrolic region at ~399.7 eV can be attributed to M–N (M = Ni, Cu), indicating that the metal predominantly bonded to N atoms in the CTF, [53–55] which was consistent with the EXAFS fitting results. In the Ni 2p core-level XPS spectra, the Ni 2p^{3/2} peaks of Ni-CTF located at ~855.7 eV corresponded to Ni²⁺. [56–58] When Cu atoms were introduced into Ni-CTF to form atom-pairs, the Ni 2p^{3/2} peak moved down by 0.8 eV to ~854.9 eV, reflecting the declining trend of the valence state of Ni due to the increased electron density surrounding it. The XPS results are similar to the XANES results, revealing a special state (0.74 +) of Ni in Ni/Cu_{0.38}-CTF. For the Cu 2p spectra, the Cu 2p^{3/2} peak for Cu-CTF was observed at ~933.4 eV, which was between that of Cu⁺ (932.3 eV) and Cu²⁺ (935.0 eV). [59] In particular, the Cu 2p^{3/2} peak moved up by 0.9 eV to ~934.3 eV when comparing Ni/Cu_{0.38}-CTF to Cu-CTF. The transition of Cu to high binding energy indicated an upward trend in the valence state and decrease in the surrounding density, revealing the electron-deficient state of the Cu site. [60] The above results show that in Ni/Cu-CTF, there was electron supply from the Cu atom to the Ni atom between the Ni-Cu atom-pairs, which was an orientation of electrons that reversed the law of electronegativity.

The calculated charge difference surfaces (Fig. 3h and Fig. S13) further revealed that electrons in Ni-CTF preferentially accumulated near Ni atoms, but the charge of Cu atoms in Cu-CTF atoms was rather local with a complete charge consumption zone surrounding it. The charge consumption area of the Cu atom was broken. Moreover, Cu atoms in the atom-pairs exhibited electron delocalization and electron accumulation in the direction of Ni atoms, as evidenced by the appearance of a Cu-to-Ni electron accumulation area. A combination of XPS, XAS, and computational simulations further confirmed the presence of electrons with a predetermined orientation in the atom-pairs from Cu to Ni. This had a significant effect on the electrocatalytic activity and stable configuration of the catalysts.

3.3. Electrocatalytic CO₂RR performance of the catalyst

To determine the optimal diatomic level, the optimal amount of the second metal Cu was investigated. The CO₂RR of a series of Ni/Cu-DACs at –0.8 V vs. RHE was examined (Fig. S19). Except for Ni/Cu_{0.07}-CTF, all Ni/Cu-DACs exhibited high CO selectivity. A series of electrochemical characterizations was performed for the evaluation of intrinsic activity. [61] According to the LSV graph (Fig. S20), the faradaic current rose as the amount of metal incorporation increased. Additionally, the currents generated by various catalysts at –1.1 V vs. RHE were measured (Fig. S21). The faraday currents were found to fit linearly with the added Cu concentrations, with R² reaching 0.976. However, the current generated by the catalyst devoid of Cu atoms deviated significantly from the fitted straight line, indicating that the CO₂RR reaction pathways of the catalyst before and after the addition of Cu atoms were distinct. After the introduction of Cu atoms, the CO₂RR may prefer to occur on adjacent Ni-Cu atom-pairs instead of single Ni atoms. The Tafel slope and electrochemical impedance spectroscopy (EIS) of Ni/Cu-DACs with varying Cu concentrations were also measured. The results (Fig. S22, S23) show that the reaction kinetics of Ni/Cu_{0.38}-CTF was the fastest. [62,63] Finally, the Cdl of each Ni/Cu-DAC was shown in Fig. S24, Cdl is proportional to the electrochemical active surface area (ECSA) under constant test settings; hence, Cdl can be used to represent

ECSA for performance comparison. However, the ECSA of Ni/Cu_{0.38}-CTF was not the largest. This may be attributed to the excessive incorporation of the second metal that caused certain Cu atoms to form single-atom sites, thereby increasing the ECSA of the catalyst. However, not all scanning response bits can produce the CO₂RR. In conclusion, this series of experiments shows that Ni/Cu_{0.38}-CTF was at an appropriate diatomic level.

To evaluate the electrochemical properties of the catalyst, LSV was performed in a 0.1 M aqueous solution of KHCO₃ saturated with CO₂ (Fig. 4a). In the LSV curve, Ni/Cu_{0.38}-CTF exhibited the lowest current onset potential, which began to separate at approximately –0.4 V vs. RHE; hence, –0.4 V vs. RHE was used as the current onset potential of the CO₂RR. Subsequent electrostatic electrolysis was performed in a bipolar chamber reactor to evaluate the reducing product. The initial CO detection potential was as low as –0.29 V vs. RHE. The CO faradaic efficiency (FE_{CO}) of the CTF, Ni-CTF, Cu-CTF, and Ni/Cu_{0.38}-CTF was further measured at various potentials between –0.4 and –1.4 V vs. RHE. As demonstrated in Fig. 4b, the maximum FE_{CO} of Ni/Cu_{0.38}-CTF reached 99.82% at –1.1 V vs. RHE. Additionally, the FE_{CO} of Ni/Cu_{0.38}-CTF from –0.8 to –1.4 V vs. RHE was > 94%. ¹H nuclear magnetic resonance characterization of the liquid products of Ni/Cu_{0.38}-CTF at –0.8 V vs. RHE during the reaction is shown in Fig. S26. No other signals besides those of water and solvent were detected, indicating that no liquid products were formed during the CO₂RR process. [64] As can be seen in Fig. 4c, in addition to Cu-CTF, the sum of the FE of the gases in the CO₂RR products of the remaining catalysts reached 100%. The FE of H₂ for several catalysts is shown in Fig. S27. Based on the LSV curve of Ni/Cu_{0.38}-CTF in N₂ and CO₂-saturated KHCO₃ solutions, in conjunction with the FE of various catalysts, it can be assumed that CO was produced via the reduction of CO₂ in the electrolyte and not the oxidation of C in the CTF. Moreover, the CO partial current density (j_{CO}) of Ni/Cu_{0.38}-CTF (7.81 mA cm^{–2} at 1.1 V vs. RHE) was superior to that of Ni-CTF, Cu-CTF, and the CTF by 2.56, 10.83, and 101.43 times, respectively (Fig. 4d). To remove the effect of metal loading on j_{CO}, the TOF of the catalyst was measured to determine the intrinsic activity of the catalytic center (in Ni/Cu-CTF, both Ni and Cu were considered active sites). As shown in Fig. 4e, Ni/Cu_{0.38}-CTF exhibited a TOF of 5116 h^{–1} at 1.1 V vs. RHE, which was 3.51 and 2.15 times that of Ni-CTF and Cu-CTF, respectively. When compared to the highest reported TOF values with corresponding FE_{CO} in the literature (Fig. 4f), Ni/Cu_{0.38}-CTF exhibited ultrahigh CO₂RR activity and CO selectivity (the closer to the upper right, the better). Moreover, Ni/Cu_{0.38}-CTF maintained ~97% of the initial FE_{CO} without significant decrease in current density after 45 h of continuous electrolysis (Fig. S28). The XRD results (Fig. S29) of Ni/Cu_{0.38}-CTF before and after catalyzing CO₂RR showed that its crystal structure was not destroyed. In conjunction with the assessment of the electrochemical performance of other electrocatalysts (Table S6), the aforementioned results demonstrated that Ni/Cu_{0.38}-CTF exhibited ultrahigh CO₂RR activity and service life. In addition, the individual metal composition of Ni/Cu_{0.38}-CTF was the lowest ever recorded.

To analyze the reaction kinetics of the as-prepared catalysts, the Tafel slope of each catalyst was measured (Fig. 4g). The Tafel slope of Ni/Cu_{0.38}-CTF was 78 mVdec^{–1}, indicating that desorption of produced CO from the surface of the catalyst comprised the RDS due to the breakthrough of the protonation energy barrier. [65] Compared to the CTF (794 mVdec^{–1}), Ni-CTF (166 mVdec^{–1}), and Cu-CTF (280 mVdec^{–1}), Ni/Cu_{0.38}-CTF had the smallest Tafel slope (78 mVdec^{–1}), indicating that the growth rate of Ni/Cu_{0.38}-CTF in terms of current density was the highest with increasing potential, confirming the improved kinetics of CO₂ to CO conversion. EIS measurements (Fig. S30, S31 and Table S7) further confirmed the increased kinetic activity of Ni/Cu_{0.38}-CTF, as its smallest radius indicated fastest electron transfer when CO₂ was reduced to CO. To further determine the cause of the accelerated kinetics of the protonation process, in situ EIS was measured and a double parallel equivalent circuit model was used to simulate the

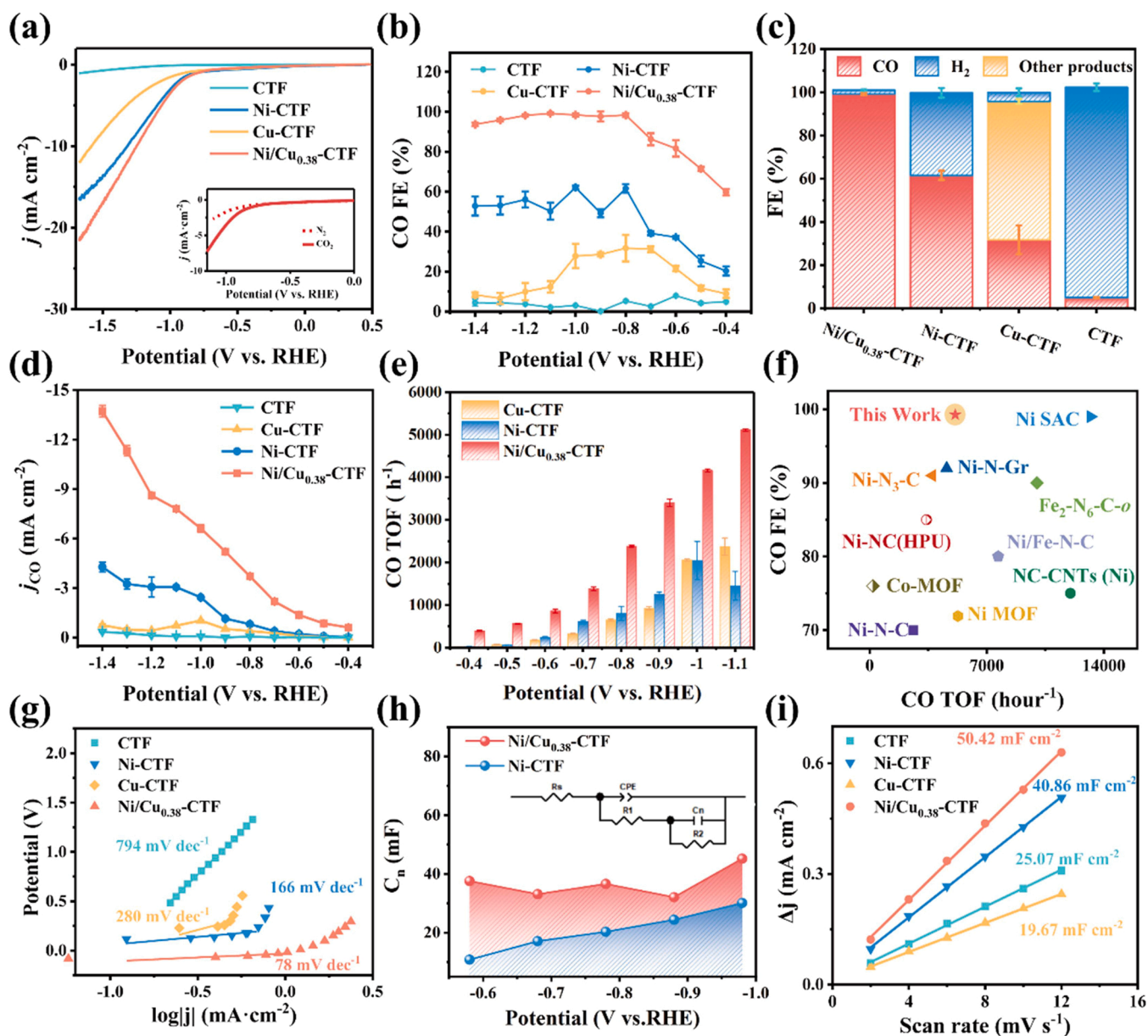


Fig. 4. (a) LSV curves of the prepared catalysts measured in CO₂-saturated 0.1 M KHCO₃ electrolyte. Inset: LSV curves of Ni/Cu_{0.38}-CTF obtained in N₂- and CO₂-saturated 0.1 M KHCO₃. (b) CO FE, (c) Proportion of products and (d) CO partial current density of the prepared catalysts. (e) Calculated TOF for Ni/Cu_{0.38}-CTF, Ni-CTF, and Cu-CTF at different applied potentials. (f) Comparison chart of the corresponding TOF values at the potential of the highest FE_{CO}. (g) Tafel diagram of CO current density and (h) Calculated C_n of Ni/Cu_{0.38}-CTF and Ni-CTF at different potentials. (i) C_{dl} of CTF, Ni-CTF, Cu-CTF and Ni/Cu_{0.38}-CTF were calculated with changes in current density and sweep rate, respectively.

Nyquist diagram (Fig. 4h). The adsorption pseudocapacitance (C_n) involving the adsorption charge of adsorbed hydrogen (*H) can be used to define the *H coverage, and the specific fitting parameters are given in Table S8. The C_n values at the same potential indicate that Ni/Cu_{0.38}-CTF had larger *H coverage than Ni-CTF. [66] Notably, when the applied potential was < 0.9 V vs. RHE, the C_n of Ni/Cu_{0.38}-CTF did not change considerably, demonstrating its intrinsic activity toward *H adsorption. Accordingly, Cu atoms can spontaneously accumulate *H from the electrolyte if sufficient protons are provided for CO₂ to form COOH.

To further compare the intrinsic activities of Ni/Cu_{0.38}-CTF, Ni-CTF, Cu-CTF, and the CTF, cyclic voltammetry (Fig. S25) was performed at various scan rates (2–12 mV s⁻¹) to determine their ECSA by calculating C_{dl}. Cu-CTF possessed lower C_{dl} than the CTF, which may be attributable to the fact that Cu-CTF possessed a smaller BET specific surface

area than the CTF (Fig. 4i). Moreover, Cu-CTF had a lower ECSA than the CTF, which was also attributable to its low concentration of metal atoms. Ni/Cu_{0.38}-CTF exhibited the largest C_{dl} (or ECSA), which corroborated its superior CO₂RR performance.

3.4. Tailoring electron orientation mechanism

To investigate the catalytic activity of the Ni-Cu atom-pairs on the CO₂RR, CO₂ adsorption models of various catalysts were first optimized using DFT (Fig. 5a). The results show that Cu-CTF has a weak potential to adsorb CO₂ on the Cu site and cannot form bonds with CO₂. This was also demonstrated by the nearly unchanged bond angle of CO₂ (179.3°). The Cu site in the Ni-Cu atom-pair may likewise lack spontaneous CO₂ adsorption, preventing it from competing with the Ni site for adsorption. This also validated the in situ EIS result that Cu atoms spontaneously

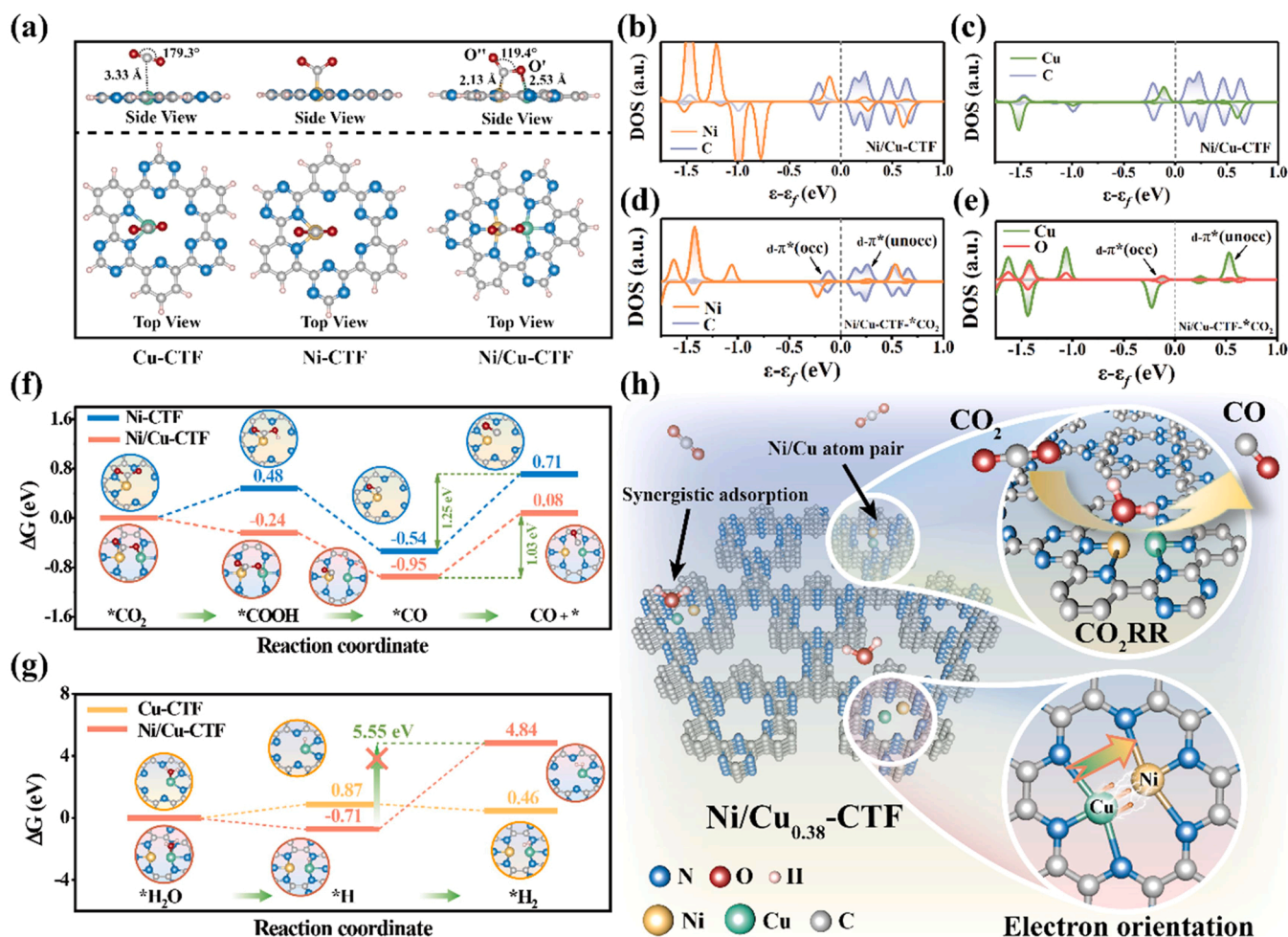


Fig. 5. (a) Optimized CO₂ adsorption configuration of Ni-CTF, Cu-CTF and Ni/Cu-CTF. The PDOS of Ni/Cu-CTF (b, c) before and (d, e) after CO₂ absorption. Gibbs free energy plots for (f) CO₂RR and (g) HER. (h) Schematic diagram of the electrocatalytic reduction of CO₂ to CO on Ni/Cu-CTF.

accumulate *H from the electrolyte. Due to the presence of Cu atoms, the adsorption of CO₂ on Ni/Cu-CTF produced proximal O (near the substrate) and distal O (away from the substrate), denoted as O' and O'', respectively. The Cu atom on Ni/Cu-CTF thus enhanced CO₂ adsorption by forming a bond with O'.

The density of states (DOS) of Ni-SACs, Cu-SACs, and Ni/Cu-DACs before and after CO₂ adsorption was calculated to further investigate the adsorption and desorption behavior of CO₂ onto active sites. Before the adsorption of CO₂ (Fig. S33a), Ni in Ni-CTF exhibited the characteristic band structure of the metal, i.e., continuous band distribution close to the Fermi energy level. In the DOS of Ni-CTF-*CO₂ (Fig. S33b), the 3d orbital of the Ni atom interacted with the π* orbital of CO₂ to form a d-π* orbital with an energy level considerably greater than the Fermi energy level. Additionally, the 3d orbitals of the Ni atom exhibited considerable overall upward shift and narrowing width. These changes demonstrate that Ni-CTF had strong adsorption capacity for CO₂, but the high energy of the d-π* (unoccupied, denoted as unocc) orbital did not facilitate the movement of electrons from the d orbital of the Ni atom to activate CO₂. Moreover, the DOS of Cu-CTF before and after the adsorption of CO₂ hardly changed (Fig. S33c, S33d), indicating that the Cu site possessed low adsorption capacity for CO₂ and relied heavily on the substrate for CO₂ adsorption to complete the CO₂RR.[67] In contrast, in Ni/Cu-CTF (Fig. 5b, c), Ni and Cu atoms interacted closely, resulting in a shift in the distribution of their d orbitals. Because of the electron-supplying properties of the pyridine nitrogen, Cu atom can obtain electron from pyridine nitrogen, so that it not only did not attract

electrons from the Ni atom (Fig. 3h), but also supplied electrons to the Ni atom. The Ni d orbitals became sharper and more concentrated, but the Cu d orbital distribution became uniform, with fewer spikes and enhanced non-local electron characteristics, which corresponded to the electron orientation of the Cu atom relative to that of the Ni atom. After the adsorption of CO₂ (Fig. 5d), the d orbital of the Ni atom in Ni/Cu-CTF moved down, indicating that its state was more stable. Under the influence of the Cu atom, the first shell of the Ni atom in the catalyst and C atom in CO₂ did not entirely overlap at the Fermi level. The decrease in overlap area of the d-π* (unocc) orbitals demonstrated that the coupling of their antibonding orbitals was reduced, although their positions remained the same. When electrons leaped above the Fermi energy level, they were more likely to enter the orbitals of the C atoms of CO₂ than the d orbitals of Ni atoms, thus reducing the energy required for CO₂ activation. As shown in Fig. 5e, where Cu d orbitals highly coincide with O p orbitals, it can be confirmed that the Cu atom works with the Ni atom to complete the adsorption of CO₂. Thus, the introduction of Cu atoms increased the adsorption of CO₂ by bonding with O atoms and decreased the antibonding orbital coupling of Ni atoms to C atoms, resulting in a greater tendency for electrons in the orbitals to enter the C atom orbitals to activate CO₂, which was advantageous for the CO₂RR.

To further examine the differences between the CO₂ reduction processes on the catalysts, the Gibbs free energy changes of the CO₂RR and HER were calculated. As shown in Fig. 5f, Ni/Cu-CTF was able to surpass the energy barrier for CO₂ activation. The twice protonations of

CO₂ on Ni/Cu-CTF exhibited a decrease in free energy spontaneity. Although the second protonation was an exothermic reaction similar to that of Ni-CTF, the lower free energy of the adsorption site of Ni/Cu-CTF rendered desorption of CO on it preferable to that on a SAC. The greater protonation energy barrier of Ni-CTF was detrimental to inhibiting the HER. The shift in free energy demonstrated that the protonation process of CO₂ on Ni/Cu-CTF was distinct from that on Ni-CTF. Accordingly, the reasons for the change in the free energy barrier were explored by optimizing the structure of the reaction process. Based on the optimized structure (Fig. S37, S38), the C–O' bond length of CO₂ adsorbed on Ni/Cu-CTF (1.22 Å) was longer than that on Ni-CTF (1.21 Å), indicating that the enhancement of CO₂ adsorption was achieved by synergistic adsorption with Cu atom. The similar C–O bond length showed that there was no obvious relationship between the breakthrough of the first protonation energy barrier and the change in adsorption configuration, also demonstrating that the electron orientation between the Ni–Cu atom-pairs played a crucial role in overcoming the protonation energy barrier. Moreover, the C–O' bond length in COOH on Ni/Cu-CTF was considerably longer than that on Ni-CTF, which was beneficial to the formation of *CO during secondary protonation as C–O' was more likely to break. The longer Ni–C bond in Ni/Cu-CTF-*CO was also consistent with the lower CO desorption barrier on Ni/Cu-CTF. Comparing the change in HER free energy at the Cu site of Ni/Cu-CTF and Cu-CTF (Fig. 5g) revealed that the free energy from *H₂O to *H on Ni/Cu-CTF decreased, but there was a large energy barrier from *H to *H₂. Therefore, a substantial amount of H would accumulate at the Cu site of Ni/Cu-CTF. When the Ni site activated CO₂, these H would participate in the protonation process of *CO₂. The presence of a tailored electron orientation in the atom-pairs left the Cu atoms in an electron-deficient state and enriched H₂O and e[−] from the electrolyte to generate *H, which was then constantly captured by activated *CO₂ for protonation without generating *H₂.

Through a series of experiments and calculations, it was proved that the Ni/Cu atom-pair catalyst was superior to SACs. When Cu atoms were introduced into a Ni SAC to form atom-pair sites with Ni atoms, the Cu atoms provide electrons to the Ni atoms to build an atom-pair catalyst with predetermined electron orientation. The effects of the determined electron orientation were mutual for the Ni and Cu atoms in the atom-pair and beneficial to the CO₂RR. In the CO₂RR process, Cu and Ni atoms in the atom-pair combined to complete the adsorption of CO₂. The presence of electron orientation weakened the Ni–C antibonding orbital coupling to enhance the adsorption of CO₂ while leaving the Cu atom electron-deficient. The former favored the activation of *CO₂, and the latter induced Cu atoms to enrich H₂O and e[−] from the electrolyte, which then produced *H. These *H did not pair to form *H₂ but were utilized in the protonation process, which substantially increased the selectivity and activity of the diatomic catalyst in the CO₂RR.

4. Conclusion

In conclusion, we have shown that electron orientation tailoring between Ni–Cu atom-pairs in Ni/Cu_{0.38}-CTF is crucial for promoting CO₂ protonation and avoiding competing reactions. The weakening of antibonding coupling between Ni atoms and CO₂ and synergistic adsorption with Cu atoms increased the adsorption and activation of CO₂. The electron-deficient Cu site served as a spontaneous enrichment center for *H, which offered an inexhaustible source of protons to overcome the kinetic barriers of intermediate protonation. Consequently, the Ni/Cu_{0.38}-CTF electrocatalyst with unique electron orientation sites exhibited excellent CO₂RR activity (5116 h^{−1}) and selectivity (99.82% for CO). This study investigated the design of atom-level reaction sites on the surface of a catalyst to facilitate competitive electrocatalytic CO₂ conversion.

CRedit authorship contribution statement

Yi Shen: Supervision, Funding acquisition, Resources, Writing – review & editing. **Haizhong Zhang:** Writing – original draft, Conceptualization, Data curation, Software. **Baoliang Chen:** Review & editing. **Zhu Chao:** Supervision, Methodology, Computational modeling, Writing & editing. **Weiting Yu:** Characterization. **Jingyi Yang:** Data curation, Software. **Qile Fang:** Computational modeling. **Zhiqiao He:** Review & editing. **Tulai Sun:** Review & editing. **Shuang Song:** Review & editing.

Declaration of Competing Interest

The authors declare that they have no known competing financial interests or personal relationships that could have appeared to influence the work reported in this paper.

Data availability

Data will be made available on request.

Acknowledgements

This research was supported by the National Natural Science Foundation of China (22276171, 22006131, 22076168, 21908199), the China Postdoctoral Science Foundation (2022M722811, 2020T130598, 2019M662106), the Zhejiang Provincial Natural Science Foundation of China (LQ20B070010), Zhuhai Science and Technology Bureau (ZH22017003210025PWC).

Appendix A. Supporting information

Supplementary data associated with this article can be found in the online version at doi:10.1016/j.apcatb.2023.122654.

References

- [1] E. Kintisch, After Paris: the rocky road ahead, *Science* 350 (2015) 1018–1019.
- [2] J. Rogelj, M. den Elzen, N. Höhne, T. Fransen, H. Fekete, H. Winkler, R.S. Chaeffer, F. Ha, K. Riahi, M. Meinshausen, Paris agreement climate proposals need a boost to keep warming well below 2 °C, *Nature* 534 (2016) 631–639.
- [3] A.A. Fawcett, G.C. Iyer, L. Clarke, J.A. Edmonds, N.E. Hultman, H. Mcjeon, J. Rogelj, R. Schuler, J. Alsalam, G.R. Asrar, J. Creason, M. Jeong, J.R. McFarland, A. Munda, W. Shi, Can Paris pledges avert severe climate change? *Science* 350 (2015) 1168–1169.
- [4] D.X. Yang, Q.G. Zhu, C.J. Chen, H.Z. Liu, Z.M. Liu, Z.J. Zhao, X.Y. Zhang, S.J. Liu, B.X. Han, Selective electroreduction of carbon dioxide to methanol on copper selenide nanocatalysts, *Nat. Commun.* 10 (2019) 677.
- [5] S. Liu, H.B. Yang, S.F. Hung, J. Ding, W.Z. Cai, L.H. Liu, J.J. Gao, X.N. Li, X.Y. Ren, Z.C. Kuang, Y.Q. Huang, T. Zhang, B. Liu, Elucidating the electrocatalytic CO₂ reduction reaction over a model single-atom nickel catalyst, *Angew. Chem. Int. Ed.* 59 (2020) 798–803.
- [6] Z.L. Jiang, T. Wang, J.J. Pei, H.S. Shang, D.N. Zhou, H.J. Li, J.C. Dong, Y. Wang, R. Cao, Z.B. Zhuang, W.X. Chen, D.S. Wang, J.T. Zhang, Y.D. Li, Discovery of main group single Sb–N₄ active sites for CO₂ electroreduction to formate with high efficiency, *Energy Environ. Sci.* 13 (2020) 2856–2863.
- [7] N. Podrojkova, V. Sans, A. Orinak, R. Orinakova, Recent developments in the modelling of heterogeneous catalysts for CO₂ conversion to chemicals, *ChemCatChem* 12 (2019) 1802–1825.
- [8] S. Jin, Z. Hao, K. Zhang, Z. Yan, J. Chen, Advances and challenges for the electrochemical reduction of CO₂ to CO: from fundamentals to industrialization, *Angew. Chem. Int. Ed.* 133 (2021) 20795–20816.
- [9] Y. Yamazaki, M. Miyaji, O. Ishitani, Utilization of low-concentration CO₂ with molecular catalysts assisted by CO₂-capturing ability of catalysts, additives, or reaction media, *J. Am. Chem. Soc.* 144 (2022) 6640–6660.
- [10] A. Goyal, G. Marcandalli, V.A. Mints, M.T.M. Koper, Competition between CO₂ Reduction and Hydrogen Evolution on a Gold Electrode under Well-Defined Mass Transport Conditions, *J. Am. Chem. Soc.* 142 (2020) 4154–4161.
- [11] J. Liu, Y.M. Cai, R.B. Song, S.C. Ding, Z.Y. Lyu, Y.C. Chang, H.Y. Tian, X. Zhang, D. Du, W.L. Zhu, Y. Zhou, Y.H. Lin, Recent progress on single-atom catalysts for CO₂ electroreduction, *Mater. Today* 48 (2021) 95–114.
- [12] H.T. Du, J.J. Fu, L.X. Liu, S.C. Ding, Z. Lyu, X. Jin, F.O. Kengara, B. Song, Q.H. Min, J.J. Zhu, D. Du, C. Gu, Y.H. Lin, J.S. Hu, W.L. Zhu, Recent progress in electrochemical reduction of carbon monoxide toward multi-carbon products, *Mater. Today* 59 (2022) 182–199.

- [13] M. Fang, L. Xu, H. Zhang, Y. Zhu, W.Y. Wong, Metalloporphyrin-linked mercurated graphynes for ultrastable CO₂ electroreduction to CO with nearly 100% selectivity at a current density of 1.2 A cm⁻², *J. Am. Chem. Soc.* 144 (2022) 15143–15154.
- [14] Y. Chen, J. Lin, B.H. Jia, X.D. Wang, S.Y. Jiang, T.Y. Ma, Isolating single and few atoms for enhanced catalysis, *Adv. Mater.* 34 (2022), 2201796.
- [15] Y. Cai, J. Fu, Y. Zhou, Y.C. Chang, Q. Min, J.J. Zhu, Y. Lin, W. Zhu, Insights on forming Ni, O-coordinated Cu single-atom catalysts for electrochemical reduction CO₂ to methane, *Nat. Commun.* 12 (2021) 586.
- [16] W. Zhu, J. Fu, J. Liu, Y. Chen, X. Li, K. Huang, Y. Cai, Y. He, Y. Zhou, D. Su, J.-J. Zhu, Y. Lin, Tuning single atom-nanoparticle ratios of Ni-based catalysts for synthesis gas production from CO₂, *Appl. Catal. B* 264 (2020), 118502.
- [17] Z. Weng, J.B. Jiang, Y.S. Wu, Z.S. Wu, X.T. Guo, K.L. Materna, W. Liu, V.S. Batista, G.W. Brudvig, H.L. Wang, Electrochemical CO₂ Reduction to Hydrocarbons on a Heterogeneous Molecular Cu Catalyst in Aqueous Solution, *J. Am. Chem. Soc.* 138 (2016) 8076–8079.
- [18] J.H. Lee, S. Kattel, Z. Jiang, Z. Xie, S. Yao, B.M. Tackett, W. Xu, N.S. Marinkovic, J. G. Chen, Tuning the activity and selectivity of electroreduction of CO₂ to synthesis gas using bimetallic catalysts, *Nat. Commun.* 10 (2019) 3724.
- [19] R. Zhao, Y. Wang, G. Ji, J. Zhong, F. Zhang, M. Chen, S. Tong, P. Wang, Z. Wu, B. Han, Z. Liu, *Adv. Mater.* 35 (2023), e2205262.
- [20] Y. Guo, S. Yao, Y. Xue, X. Hu, H. Cui, Z. Zhou, Nickel single-atom catalysts intrinsically promoted by fast pyrolysis for selective electroreduction of CO₂ into CO, *Appl. Catal. B* 304 (2022), 120997.
- [21] H.B. Yang, S.-F. Hung, S. Liu, K. Yuan, S. Miao, L. Zhang, X. Huang, H.-Y. Wang, W. Cai, R. Chen, J. Gao, X. Yang, W. Chen, Y. Huang, H.M. Chen, C.M. Li, T. Zhang, B. Liu, Atomically dispersed Ni(i) as the active site for electrochemical CO₂ reduction, *Nat. Energy* 3 (2018) 140–147.
- [22] P. Su, K. Iwase, T. Harada, K. Kamiya, S. Nakanishi, Covalent triazine framework modified with coordinatively-unsaturated Co or Ni atoms for CO₂ electrochemical reduction, *Chem. Sci.* 9 (2018) 3941–3947.
- [23] Q. Fan, P. Hou, C. Choi, T.S. Wu, S. Hong, F. Li, Y.L. Soo, P. Kang, Y. Jung, Z. Sun, Activation of Ni Particles into Single Ni–N Atoms for Efficient Electrochemical Reduction of CO, *Adv. Energy Mater.* 10 (2019), 1903068.
- [24] C. Liu, T. Li, X. Dai, J. Zhao, D. He, G. Li, B. Wang, X. Cui, Catalytic activity enhancement on alcohol dehydrogenation via directing reaction pathways from single- to double-atom catalysis, *J. Am. Chem. Soc.* 144 (2022) 4913–4924.
- [25] Z. Zeng, L.Y. Gan, H. Bin Yang, X. Su, J. Gao, W. Liu, H. Matsumoto, J. Gong, J. Zhang, W. Cai, Z. Zhang, Y. Yan, B. Liu, P. Chen, Orbital coupling of hetero-diatom nickel-iron site for bifunctional electrocatalysis of CO₂ reduction and oxygen evolution, *Nat. Commun.* 12 (2021) 4088.
- [26] F.H. Wang, H.P. Xie, T. Liu, Y.F. Wu, B. Chen, Highly dispersed CuFe-nitrogen active sites electrode for synergistic electrochemical CO₂ reduction at low overpotential, *Appl. Energy* 269 (2020), 115029.
- [27] Y. Wang, B.J. Park, V.K. Paidi, R. Huang, Y. Lee, K.-J. Noh, K.-S. Lee, J. W. Han, Precisely constructing orbital coupling-modulated dual-atom Fe pair sites for synergistic CO₂ electroreduction, *ACS Energy Lett.* 7 (2022) 640–649.
- [28] W.J. Zhu, L. Zhang, S.H. Liu, A. Li, X.T. Yuan, C.L. Hu, G. Zhang, W.Y. Deng, K. T. Zang, J. Luo, Y.M. Zhu, M. Gu, Z.J. Zhao, J.L. Gong, Enhanced CO₂ electroreduction on neighboring Zn/Co monomers by electronic effect, *Angew. Chem. Int. Ed.* 59 (2020) 12664–12668.
- [29] L. Zhang, J. Feng, S. Liu, X. Tan, L. Wu, S. Jia, L. Xu, X. Ma, X. Song, J. Ma, X. Sun, B. Han, Atomically Dispersed Ni–Cu Catalysts for pH-Universal CO₂ Electroreduction, *Adv. Mater.* (2023), e2209590.
- [30] X. Li, S.-G. Han, W. Wu, K. Zhang, B. Chen, S.-H. Zhou, D.-D. Ma, W. Wei, X.-T. Wu, R. Zou, Q.-L. Zhu, Convergent paired electrosynthesis of dimethyl carbonate from carbon dioxide enabled by designing the superstructure of axial oxygen coordinated nickel single-atom catalysts, *Energy Environ. Sci.* 16 (2023) 502–512.
- [31] H. Cheng, X. Wu, M. Feng, X. Li, G. Lei, Z. Fan, D. Pan, F. Cui, G. He, Atomically dispersed Ni/Cu dual sites for boosting the CO₂ reduction reaction, *ACS Catal.* 11 (2021) 12673–12681.
- [32] T. Zheng, K. Jiang, N. Ta, Y. Hu, J. Zeng, J. Liu, H. Wang, Large-scale and highly selective CO₂ electrocatalytic reduction on nickel single-atom catalyst, *Joule* 3 (2019) 265–278.
- [33] J. Zhu, M. Xiao, D. Ren, R. Gao, X. Liu, Z. Zhang, D. Luo, W. Xing, D. Su, A. Yu, Z. Chen, Quasi-Covalently Coupled Ni–Cu Atomic Pair for Synergistic Electroreduction of CO₂, *J. Am. Chem. Soc.* 144 (2022) 9661–9671.
- [34] G. Kresse, J. Furthmüller, Efficiency of ab-initio total energy calculations for metals and semiconductors using a plane-wave basis set, *Comp. Mater. Sci.* 6 (1996) 15–50.
- [35] G. Kresse, J. Furthmüller, Efficient iterative schemes for ab initio total-energy calculations using a plane-wave basis set, *Phys. Rev. B* 54 (1996) 11169–11186.
- [36] G. Kresse, D. Joubert, From ultrasoft pseudopotentials to the projector augmented-wave method, *Phys. Rev. B* 59 (1999) 1758–1775.
- [37] J.P. Perdew, K. Burke, M. Ernzerhof, Generalized gradient approximation made simple, *Phys. Rev. Lett.* 77 (1996) 3865–3868.
- [38] J.P. Perdew, M. Ernzerhof, K. Burke, Rationale for mixing exact exchange with density functional approximations, *J. Chem. Phys.* 105 (1996) 9982–9985.
- [39] K. Iwase, T. Yoshioka, S. Nakanishi, K. Hashimoto, K. Kamiya, Copper-modified covalent triazine frameworks as non-noble-metal electrocatalysts for oxygen reduction, *Angew. Chem. Int. Ed.* 54 (2015) 11068–11072.
- [40] K. Kamiya, R. Kamai, K. Hashimoto, S. Nakanishi, Platinum-modified covalent triazine frameworks hybridized with carbon nanoparticles as methanol-tolerant oxygen reduction electrocatalysts, *Nat. Commun.* 5 (2014) 5040.
- [41] Z. Cheng, W. Fang, T.S. Zhao, S.Q. Fang, J.H. Bi, S.J. Liang, L.Y. Li, Y. Yu, L. Wu, Efficient Visible-Light-Driven Photocatalytic Hydrogen Evolution on Phosphorus-Doped Covalent Triazine-Based Frameworks, *ACS Appl. Mater. Inter.* 10 (2018) 41415–41421.
- [42] K. Sakaushi, M. Antonietti, Carbon- and nitrogen-based organic frameworks, *Acc. Chem. Res.* 48 (2015) 1591–1600.
- [43] Y. Gang, F.P. Pan, Y.H. Fei, Z.C. Du, Y.H. Hu, Y. Li, Highly efficient nickel, iron, and nitrogen codoped carbon catalysts derived from industrial waste petroleum coke for electrochemical CO₂ reduction, *ACS Sustain. Chem. Eng.* 8 (2020) 8840–8847.
- [44] L.C. Bai, C.S. Hsu, D.T.L. Alexander, H.M. Chen, X.L. Hu, A. Cobalt-Iron, Double-atom catalyst for the oxygen evolution reaction, *J. Am. Chem. Soc.* 141 (2019) 14190–14199.
- [45] H.Y. Cheng, X.M. Wu, X.C. Li, Y.Y. Zhang, M.M. Feng, Z.H. Fan, G.H. He, Zeolitic imidazole framework-derived FeN₅-doped carbon as superior CO₂ electrocatalysts, *J. Catal.* 395 (2021) 63–69.
- [46] P. Li, M. Wang, X. Duan, L. Zheng, X. Cheng, Y. Zhang, Y. Kuang, Y. Li, Q. Ma, Z. Feng, W. Liu, X. Sun, Boosting oxygen evolution of single-atomic ruthenium through electronic coupling with cobalt-iron layered double hydroxides, *Nat. Commun.* 10 (2019) 1711.
- [47] C. Zhu, L. Lu, Q. Fang, S. Song, B. Chen, Y. Shen, Unveiling spin state-dependent micropollutant removal using single-atom covalent triazine framework, *Adv. Funct. Mater.* (2023), <https://doi.org/10.1002/adfm.202210905>.
- [48] Z. Kong, L. Lu, C. Zhu, J. Xu, Q. Fang, R. Liu, Y. Shen, Enhanced adsorption and photocatalytic removal of PFOA from water by F-functionalized MOF with in-situ-growth TiO₂: Regulation of electron density and bandgap, *Sep. Purif. Technol.* 297 (2022), 121449.
- [49] J. Xu, L. Lu, C. Zhu, Q. Fang, R. Liu, D. Wang, Z. He, S. Song, Y. Shen, Insights into conduction band flexibility induced by spin polarization in titanium-based metal-organic frameworks for photocatalytic water splitting and pollutants degradation, *J. Colloid Interf. Sci.* 630 (2023) 430–442.
- [50] Y. Shen, Y. Yao, L. Lu, C. Zhu, Q. Fang, J. Wang, S. Song, Insights into dual effect of missing linker-cluster domain defects for photocatalytic 2e⁻ ORR: Radical reaction and electron behavior, *Chemosphere* 324 (2023), 138220.
- [51] J. Xu, C. Zhu, S. Song, Q. Fang, J. Zhao, Y. Shen, A nanocubicle-like 3D adsorbent fabricated by in situ growth of 2D heterostructures for removal of aromatic contaminants in water, *J. Hazard. Mater.* 433 (2022), 127004.
- [52] Y. Shen, S. Liu, L. Lu, C. Zhu, Q. Fang, R. Liu, Y. Shen, S. Song, Pyridine-linked covalent triazine frameworks with bidirectional electron donor-acceptor for efficient organic pollution removal, *J. Hazard. Mater.* 444 (2023), 130428.
- [53] Y. Yang, C.L. Wang, S.Q. Gao, K.T. Mao, G.L. Xia, Z.Y. Lin, P. Jiang, L. Hu, Q. W. Chen, Incorporation of Cu-N_x cofactors into graphene encapsulated Co as biomimetic electrocatalysts for efficient oxygen reduction, *Nanoscale* 10 (2018) 21076–21086.
- [54] X. Yang, J. Cheng, B.Z. Fang, X.X. Xuan, N. Liu, X. Yang, J.H. Zhou, Single Ni atoms with higher positive charges induced by hydroxyls for electrocatalytic CO₂ reduction, *Nanoscale* 12 (2020) 18437–18445.
- [55] C. Zhu, L. Lu, J.J. Xu, S. Song, Q.L. Fang, R.L. Liu, Y.X. Shen, J.K. Zhao, W. Dong, Y. Shen, Metal monovacancy-induced spin polarization for simultaneous energy recovery and wastewater purification, *Chem. Eng. J.* 451 (2023), 138537.
- [56] Y.N. Gong, L. Jiao, Y.Y. Qian, C.Y. Pan, L.R. Zheng, X.C. Cai, B. Liu, S.H. Yu, H. L. Jiang, Regulating the Coordination Environment of MOF-Templated Single-Atom Nickel Electrocatalysts for Boosting CO₂ Reduction, *Angew. Chem. Int. Ed.* 59 (2020) 2705–2709.
- [57] Z.J. Ma, X.L. Zhang, D.P. Wu, X.Y. Han, L.M. Zhang, H.J. Wang, F. Xu, Z.Y. Gao, K. Jiang, Ni and nitrogen-codoped ultrathin carbon nanosheets with strong bonding sites for efficient CO₂ electrochemical reduction, *J. Colloid Interf. Sci.* 570 (2020) 31–40.
- [58] T. Zhang, D. Zhang, X.H. Han, T. Dong, X.W. Guo, C.S. Song, R. Si, W. Liu, Y.F. Liu, Z.K. Zhao, Preassembly Strategy To Fabricate Porous Hollow Carbonitride Spheres Inlaid with Single Cu–N₃ Sites for Selective Oxidation of Benzene to Phenol, *J. Am. Chem. Soc.* 144 (2022), 1066–1066.
- [59] Q.X. Lai, J.J. Zhu, Y.X. Zhao, Y.Y. Liang, J.P. He, J.H. Chen, MOF-Based Metal-Doping-Induced Synthesis of Hierarchical Porous Cu–N/C Oxygen Reduction Electrocatalysts for Zn–Air Batteries, *Small* 13 (2017), 1700740.
- [60] Z.H. Xiao, Y. Wang, Y.C. Huang, Z.X. Wei, C.L. Dong, J.M. Ma, S.H. Shen, Y.F. Li, S. Y. Wang, Filling the oxygen vacancies in Co₃O₄ with phosphorus: an ultra-efficient electrocatalyst for overall water splitting, *Energy Environ. Sci.* 10 (2017) 2563–2569.
- [61] Z.G. Geng, Y.J. Cao, W.X. Chen, X.D. Kong, Y. Liu, T. Yao, Y. Lin, Regulating the coordination environment of Co single atoms for achieving efficient electrocatalytic activity in CO₂ reduction, *Appl. Catal. B-Environ.* 240 (2019) 234–240.
- [62] W. Kou, Y.X. Zhang, J. Dong, C.H. Mu, L.B. Xu, Nickel-Nitrogen-Doped Three-Dimensional Ordered Macro/Mesoporous Carbon as an Efficient Electrocatalyst for CO₂ Reduction to CO, *ACS Appl. Energy Mater.* 3 (2020) 1875–1882.
- [63] C. Jia, K. Ching, P.V. Kumar, C. Zhao, N. Kumar, X.J. Chen, B. Das, Vitamin B₁₂ on graphene for highly efficient CO₂ electroreduction, *ACS Appl. Mater. Inter.* 12 (2020) 41288–41293.
- [64] Z.S. Chen, G.X. Zhang, L. Du, Y. Zheng, L.X. Sun, S.H. Sun, Nanostructured cobalt-based electrocatalysts for CO₂ reduction: recent progress, challenges, and perspectives, *Small* 16 (2020), 2004158.

- [65] L. Zhang, Z.J. Zhao, J.L. Gong, Nanostructured Materials for Heterogeneous Electrocatalytic CO₂ Reduction and their Related Reaction Mechanisms, *Angew. Chem. Int. Ed.* 56 (2017) 11326–11353.
- [66] S. Chen, X. Li, C.W. Kao, T. Luo, K. Chen, J. Fu, C. Ma, H. Li, M. Li, T.S. Chan, M. Liu, Unveiling the Proton-Feeding Effect in Sulfur-Doped Fe-N-C Single-Atom Catalyst for Enhanced CO₂ Electroreduction, *Angew. Chem. Int. Ed.* 61 (2022), e202206233.
- [67] L. Gong, X. Wang, T. Zheng, J. Liu, J. Wang, Y.-C. Yang, J. Zhang, X. Han, L. Zhang, Z. Xia, Catalytic mechanism and design principle of coordinately unsaturated single metal atom-doped covalent triazine frameworks with high activity and selectivity for CO₂ electroreduction, *J. Mater. Chem. A* 9 (2021) 3555–3566.